Hollow-adjustable polymer microneedles for prolonged hypoglycemic effect on diabetic rats

Tianqi Liu [a,b], Yanfang Sun [c,*], Wenjing Zhang [a,b], Rui Wang [a,b], Xinyu Lv [a,b], Lei Nie,[d] Amin Shavandi,[e] Khaydar E. Yunusov,[f] Guohua Jiang [a,b,*]

[a] *School of Materials Science and Engineering, Zhejiang Sci-Tech University, Hangzhou, 310018, China*

[b] *International Scientific and Technological Cooperation Base of Intelligent Biomaterials and Functional Fibers, Hangzhou, 310018, China*

[c] *College of Life Sciences and Medicine, Zhejiang Sci-Tech University, Hangzhou, Zhejiang, 310018, China*

[d] *College of Life Sciences, Xinyang Normal University, Xinyang 464000, China*

[e] *Université libre de Bruxelles (ULB), École polytechnique de Bruxelles, 3BIO10 BioMatter, Avenue F.D. Roosevelt, 50 - CP 165/61, 1050 Brussels, Belgium*

[f] *Institute of Polymer Chemistry and Physics, Uzbekistan Academy of Sciences, Tashkent, 100128, Uzbekistan*

E-mail: ghjiang_cn@zstu.edu.cn (G. Jiang)

katherineyfs@zzstu.edu.cn (Y. Sun)

Abstract: Maintaining blood glucose levels within a safe range is critical for diabetic management. In recent decades, microneedles (MNs) have emerged as a potential method for delivering drugs to treat diabetes. However, insufficient drug loading and the complexity of achieving long-acting release have presented challenges that research has not addressed well. In this study, the hollow-adjustable biocompatible polymer MNs with varying cavity volumes were developed by cyclic freeze-thawing technique. The structure of shell-layer of hollow MNs was optimized with a sequential casting approach for regulating drug release kinetics. This design can ensure the sufficient mechanical strength of MNs and help to improve the drug-loading capacity, thereby solving the problem of low drug-loading capacity and short pharmacodynamic action time of traditional polymer MNs. *In vivo* experiments performed on diabetic rat models revealed the potential of the as-fabricated MNs to effectively pierce into the skin, leading to a notable hypoglycemic effect lasting up to 14 h without inducing the risk of hypoglycemia. These results indicate that the fabricated hollow-adjustable polymer MNs is a potential candidate for transdermal delivery of high-dose drugs.

Keyword: Microneedles; transdermal delivery; diabetes; hypoglycemic effect

Graphic Abstract
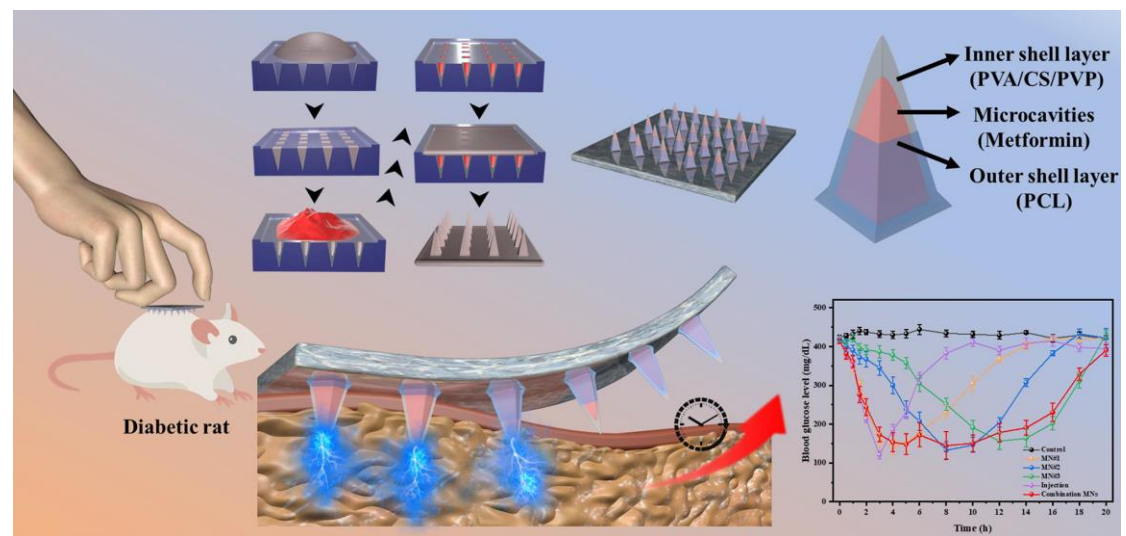
1. Introduction

Diabetes mellitus is a chronic disease marked by abnormal blood glucose levels (BGLs) due to a lack of insulin regulation. This may result into numerous complications, including chronic wound, retinopathy, nephropathy, amputation and neuropathy with failure of glucose [1-4]. The number of people affected by diabetes worldwide has risen to 537 million in 2021, and will continue to rise to 783 million by 2045 [5]. The routine management of BGLs in diabetes patients is the administration of hypoglycemic drugs, such as insulin, metformin etc., which can be delivered via oral or subcutaneous injection [6-7]. Despite its convenience, oral administration remains susceptible to the liver's first-pass effect [8]. In comparison to oral administration, subcutaneous injection is a commonly employed method for delivering a variety of hypoglycemic drugs [9]. Subcutaneous injection provides a direct route for hypoglycemic drug delivery to subcutaneous tissues and blood vessels, avoiding the elimination of drugs by the liver and intestines [10]. However, pain, bleeding and fear caused by frequent subcutaneous injections lead to poor compliance and experience of patients [11-12]. To mitigate the negative and inconvenient aspects of subcutaneous and oral drug administration and improve patient compliance, the development of a non-invasive drug delivery system is crucially necessary for effectively regulating BGLs of diabetics. As a promising transdermal drug delivery system, microneedles (MNs) have received extensive attention due to the ability to effectively deliver drugs through the stratum corneum of the skin [13-14]. MNs can improve patient compliance and experience due to the limited needle length not

touching the subcutaneous nerves [15]. MNs are generally divided into solid MNs, coated MNs, hollow MNs, dissolvable MNs and hydrogel MNs according to the location of the drug [16]. Generally, the two drug-loaded MNs categories include dissolvable MNs and hydrogel MNs have demonstrated promising efficacy in promoting hair regrowth [17], treating tumors [18] and wounds [19], and diabetes treatment [20]. As the ideal transdermal delivery platform, dissolving MNs can create microchannels in both the epidermis and dermis layers with minimal invasiveness, allowing for the efficient transdermal delivery of various sizes of nanoparticles and drugs [21]. Although MNs exhibit promising potential for localized drug delivery, the capacity to load drugs into traditional MNs is restricted by their small microstructure volume. In addition, diabetes treatment differs from other diseases as it typically involves long-term drug administration to maintain stable BGLs levels [22]. However, the MNs currently used in the treatment of diabetes can only maintain the hypoglycemic effect for a few hours, which is inadequate compared to the efficacy of oral administration that can last for more than 10 h [23-24]. Hence, it is essential to develop a MNs system that can effectively regulate BGLs for the maximum possible duration. Currently, two approaches have been adopted to achieve this goal, including responsive release and increasing drug loading while expanding drug release time [25-26]. A few studies have developed responsive release MNs patches, aiming to achieve a sustained and controlled drug release profile [27-29]. PCL MNs loaded with a photothermal agent (Prussian nanoparticles) exhibited drug melt and release characteristics under near-infrared light irradiation, which achieved photo-responsive

drug release [30]. The approach represents an innovative strategy for controlled drug delivery. Moreover, temperature-responsive [31-32], magnetic-responsive [33-34], and electrically responsive [35-36] MNs also have been proposed as novel drug-release strategies, enabling controlled drug release in response to external conditions. On the other hand, the coexisting biological responsive release MNs utilize specific reactant molecules to recognize and trigger drug release, offering superior closed-loop therapeutic control to conventional drug delivery approaches [37]. A typical glucose-responsive MNs system consists of glucose sensing components, such as glucose-binding protein (GBP) [38-39], glucose oxidase (GOx) [40-41] or phenylboronic acid (PBA) [42-43]. Various related designs, including gels [44], nanoparticles [45-46], and self-assemblies [47], have been investigated to regulate BGLs *in vivo*. Glucose-responsive MNs have emerged as a promising approach for BGLs regulation. However, the reported glucose-responsive MNs are still faced with the challenges of complicated drug loading process or limited hypoglycemic effect [41].

An alternative approach is to enhance the drug loading capacity of MNs and combine multiple drug release kinetics. This strategy represents a promising opportunity for developing more efficient and effective drug delivery systems. To improve the drug loading capacity of MNs, the MNs patch backing has been explored as a "drug warehouse", thereby enhancing the loading capacity of metformin to 100 mg [48]. This technology offers a simplified one-step application process, however, the drugs in patch backing are difficult to fully utilize, thereby reducing the utilization rate of the drugs. Hollow MNs possess a lumen, or internal bore, which enables the

loading of drugs, thus offering a huge potential to enhance the loading capacity of drugs [49-50]. The hollow MNs are convenient for the delivery of multiple drug doses or allow diverse drug-release kinetics, thereby enabling sustained drug release and enhancing the effectiveness of drug therapy [51-52]. The incorporation of drug-loading cavities in the design of MNs has proven to be an effective strategy for increasing drug loading capacity. However, these works on hollow MNs made of polymers required expensive and requires complex manufacturing processes, such as laser and etching, and multi-mold fabrication, which greatly limits their development.

In this study, the hollow-adjustable biocompatible polymer MNs with varying cavity volume were fabricated by cyclic freeze-thawing technique for improving the drug-loading capacity and extending the hypoglycemic time. The MNs are comprised of three layers: an outer hydrophobic shell made of polycaprolactone (PCL), an inner hydrogel shell made of polyvinyl alcohol/chitosan/polyvinylpyrrolidone (PVA/CS/PVP, PCP), and a hollow cavity for loading metformin drug, as shown in Figure 1A. The outer hydrogel shell serves to modulate MNs core size and thereby adjust drug loading capacity, while the height of the middle hydrophobic shell can be tailored to modulate drug release kinetics. The as-fabricated MNs exhibiting distinct drug-release kinetics can be combined on a single patch to achieve multi-timepoint drug delivery, offering a promising approach to enhance drug efficacy and improve convenience and compliance for patients (Figure 1B). The hollow-adjustable MNs exhibit excellent mechanical properties and extended hypoglycemic effects, representing a promising approach to improving the treatment efficacy for diabetic

patients.
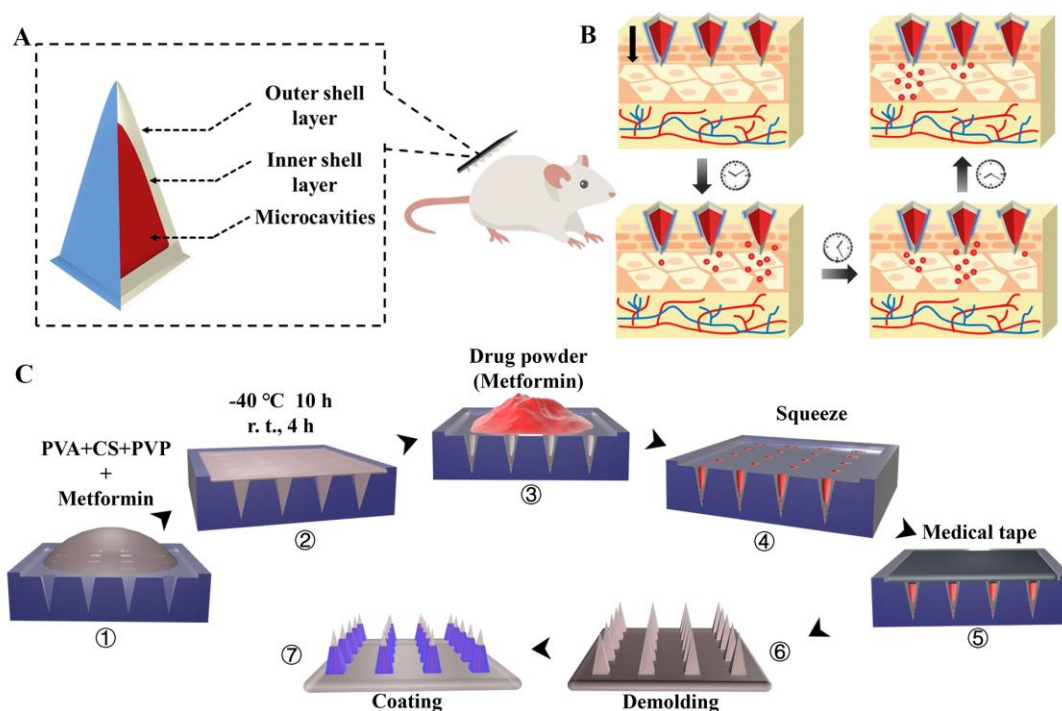
Figure 1. Schematic illustration of hollow-adjustable MNs for prolonged hypoglycemic effect on diabetic rats. The structure diagram of hollow-adjustable MNs (A), hollow-adjustable MNs after loading drugs for prolonged hypoglycemic effect on diabetic rats (B) and schematic illustration for the fabrication of hollow-adjustable MNs (C).

2. Materials and methods

2.1 Materials

Chitosan (CS), polyvinyl alcohol (PVA, alcoholysis = 99.0-99.4 mol %), polyvinylpyrrolidone (PVP, Mw = 130 kDa), and polycaprolactone (PCL, Mw = 70-90 kDa) were purchased from Aladdin Bio-chemical Technology Co., Ltd. (Shanghai, China). Acetic acid (HPLC, ≥99.9%), rhodamine 6G (R6G), and fluorescein isothiocyanate (FITC) were obtained from Mclean Bio-chemical Technology Co., Ltd. (Shanghai, China). 3-(4,5-Dimethyl-2-thiazolyl)-2,5-diphenyl tetrazolium bromide (MTT) was purchased from Beyotime Biotechnology Co., Ltd. (Shanghai, China). Rat Metformin Hydrochlorideelisa Kit was purchased from

Shanghai Baililai Biotechnology Co., Ltd. All reagents employed were of analytical grade and used without further purification.

2.2 Synthesis and characterizations of PCP hydrogel

The polyvinyl alcohol/chitosan/polyvinylpyrrolidone (PCP) mixed solution was prepared as the matrix of MNs inner shell according to the previously reported method [53]. Briefly, a 15 wt% PVA solution was obtained by dissolving PVA in deionized water at 90 °C for 6 h. Subsequently, varied amounts of PVP were dissolved in the PVA solution, while CS was dissolved in acetic acid at room temperature to obtain a 2 wt% solution through continuous stirring. After mixing and stirring, two solutions with different PCP ratios (PCP = 4/1/1~ 4/1/4) were obtained. The PCP hydrogel was prepared by three cycles of freezing at -20 °C for 10 h followed by thawing at room temperature for 4 h. In addition, pure PVA hydrogel was also prepared through the same process.

The chemical structure of PCP was studied by Fourier transform infrared (FT-IR), and the morphology of PVA and PCP was investigated by scanning electron microscopy (SEM, JSM-7500F, JEOL, Japan). To assess the swelling degrees of the crosslinked PCP hydrogel, samples measuring $8\times8\times1$ mm³ were prepared. After lyophilization, the samples were immersed in PBS at 37 °C and taken out at intervals of 0.5, 1, 2, and 24 h. To measure the swelling degree, the patches were weighed at a designated time after removing the surface water with filter papers. After 24 h, the patches underwent another round of lyophilization before being weighed. The swelling ratio was calculated using the following equation:

$$\text{Swelling Degrees (\%)} = \frac{m_t - m_0}{m_0} \times 100\%$$

Where m_t and m_0 are the weight of hydrogels on t h and 0 h, respectively.

2.3 Fabrication of hollow-adjustable MNs

Pyramid-shaped MNs mold with a square base of 250 μm ✕ 250 μm and a height of 750 μm were arranged in a 39 × 39 array, featuring a center-to-center spacing of 300 μm, on a 4 × 4 cm² patch.

The schematic illustration in Figure 1C describes the micro-molding method to fabricate the hollow-adjustable MNs. Firstly, different amounts of PCP matrix solution (2, 4, 6, 8 mL) were poured into the PDMS female mold and filled up the cavities with centrifugation (8,000 rpm for 3 min). Subsequently, the MNs mold filled with matrix solution was subjected to freezing at -40 °C for 10 h and thawed for 4 h at room temperature. This freeze-thaw cycle was repeated three times to achieve the formation of the PCP hydrogel. Then, the MNs patch with cavities structure was formed due to the shrinkage of PCP hydrogel. The metformin powder was loaded into the cavities of MNs by squeezing. To encapsulate the drug and provide a flexible substrate, adhesive medical tape was applied to the MNs backing. After demolding, the MNs were dipped with 60 °C hot-melt PCL and placed horizontally in a 60 °C oven to form a PCL hydrophobic shell-layer outside of MNs. The The composition and structure for different MNs groups are shown in Table S1.

2.4 Mechanical and insertion properties of MNs *in vitro*

The mechanical properties of the MNs were evaluated using a universal material testing machine (5943 MicroTester, Instron, American). The MNs were positioned

horizontally on the stainless steel plate of the machine, and the pressure sensor pressed the MNs at a speed of 1 mm/s with an axial force.

To determine the insertion properties, the MNs were inserted into eight layers of simulated skin (Parafilm M film) and biological skin tissues (fresh pigskin without hair) with the universal material testing machine, respectively. After the insertion, the MNs and each layer of simulated skin were carefully separated, and the perforation situation on each layer of membrane was recorded. The punctured pigskin was examined for insertion using a microscope. Additionally, skin slices were observed using confocal laser microscopy to analyze their diffusion (C2, Nikon, Japan).

2.5 Hypoglycemic effect *in vivo*

All animal procedures were approved by the Animal Ethics Committee of Zhejiang Sci-Tech University (acceptance number, 20230314013) and performed at the Hangzhou Moslet Biotechnology Co., Ltd. Healthy male SD rats (~200 g, Beijing Weitong Lihua Experimental Animal Technology Co., Ltd) were used in this study. The SD rats were used for the subsequent experiments upon the successful establishment of the type 2 diabetes model according to previous animal modeling methods [55]. The MNs were directly inserted into the skin after they were anesthetized. To evaluate the hypoglycemic effect of MNs, the rats were randomly divided into the following six groups: (a) an untreated hyperglycemia group (negative control); (b) an injection group (SC injection, positive control, 15 mg); (c) MNs#1 group (height of PCL shell: 0 μm); (d) MNs#2 group (height of PCL shell: 200 μm); (e) MNs#3 group (height of PCL shell: 500 μm); (f) MNs#4 group (One-third MNs with PCL shell

height at 0, 200 and 500 μm) (n = 5 per group). The MNs were continuously applied for 24 h after being fixed by medical tape. The BGLs within 20 h after administration were recorded. A blood glucose meter was used to test BGLs at the predetermined time. In addition, the efficiency of regulation in SD rats with a traditional breakfast-lunch-dinner lifestyle in the MNs#4 group was also evaluated. Accordingly, the blood samples were collected to measure metformin content in blood with a metformin ELISA Kit.

2.6 Histological and immunohistochemical analyses

To assess the safety implications of microneedle administration, skin tissues and organs of rats were subjected to histological analysis. After the rats were executed, the skin tissue of the rats was fixed with paraformaldehyde and embedded in paraffin for further study. The skin tissue sections and main organs were stained using hematoxylin-eosin (H&E) staining techniques. Immunohistochemical sections stained by IF-6 were used to evaluate the inflammation of the skin. All slices were analyzed and scanned using a scanner.

3   Results and discussion

3.1 Synthesis and characterizations of PCP hydrogel

In this study, PVA, CS and PVP are selected as the matrix materials of MNs due to their biocompatibility and chemical inertness. More importantly, PVA forms micro- or submicrocrystalline domains as the cross-linking junctions by a freeze-thaw treatment under a mild condition [56-57]. These micro- or submicrocrystalline domains playing the role of knots in the gel network can improve the stability and elasticity of

the resultant PCP hydrogel, as shown in Figure 2A. It is found that the obtained PCP mixed solution without freeze-thaw process possesses a transparent sol state. After freeze-thaw treatment, the gel state can be formed (Figure 2B).

Due to the increased cross-linking density resulting from the freeze-thaw treatment, the hydrogel's stiffness will be enhanced, which contributes to providing the MNs with suitable mechanical strength.[58] Figures 2C and D illustrate the microstructure of PVA and PCP after the freeze-thaw cycle. Figure S1 shows the pore size distribution of PVA and PCP hydrogels that obtained from BET tests. PCP hydrogels exhibit a larger porous structure with average diameter at 30.75 nm in comparison with the PVA with average diameter at 13.73 nm. The relative higher crosslinking density in PVA results in a smaller pore size in the resultant hydrogel. However, in the case of a PCP hydrogel, the introduction of CS and PVP may lead to a decrease in the crosslinking density, which is partly enlarge the pore size of the composite hydrogel [59]. The large pore structure in hydrogels facilitates water penetration, leading to an effective release of drugs.

The self-crosslinking of PVA after freeze-thaw treatment was confirmed by FTIR test. As shown in Figure S2, the characteristic absorption peaks at 3446 and 1651 cm^{-1} attributed to O-H and N-H, respectively. C=O stretching is shifted to lower frequencies in the composite hydrogel, indicating strong hydrogen bonding [60-61]. To investigate phase composition in the composite hydrogel, XRD is used to test samples with or without freeze-thaw treatment. As shown in Figure 2E, the PVA hydrogel subjected to freeze-thaw treatment exhibits a sharp diffraction peak at $2\theta = 19.6°$ and

a shoulder-peak at $2\theta = 22.6°$, which is related to the (101) and (200) crystal plane of PVA [62-63]. However, only a weak diffraction peak at ~19.6° can be observed for PVA powder without freeze-thaw treatment, which confirms an increase in the crystalline nature of PVA [64]. In the PCP composite hydrogel, the characteristic peak of PVA at ~19.6° remains discernible. Additionally, a slight reduction in the shoulder-peak at $2\theta = 22.6°$ is evident. This decrease can be due to the formation of intermolecular hydrogen bonds between PVA and CS or PVP chains, leading to form new crosslinkages and 3D networking structure of hydrogel during the freeze-thawing process [65-66].

These intermolecular hydrogen bonds hinder the formation of hydrogen bonds within the PVA molecular chain itself, thereby leading to a slight reduction in crystallinity [59]. Interestingly, the structure of MNs exhibits an inward shrinkage during the preparation using PVA as the matrix. This shrinkage can be attributed to the presence of numerous crystalline regions in the PVA molecular chain [67], which generates internal stress and leads to the volume shrinkage of PVA matrix without cavity formation (Figure 2F and H). However, in the case of PCP composite matrix, a cavity structure in the central of MNs can be formed by an outward shrinkage process. The resulting MNs showed a negligible morphological change in comparison with MNs' mold [68], as shown in Figures 2G and I. This phenomenon can be attributed to decreasing binding force among PVA chains after adding CS and PVP. The weakened binding force facilitates the movement of the PVA molecular chain. In addition, during the freeze-thaw process, the composite matrix of MNs is in contact with the

mold, and a layer of frozen polymer material (skin layer) will be formed. The rapid solidification of the skin layer hinders the filling of the micro-features and can lead to incomplete filling and form a hollow structure [69].
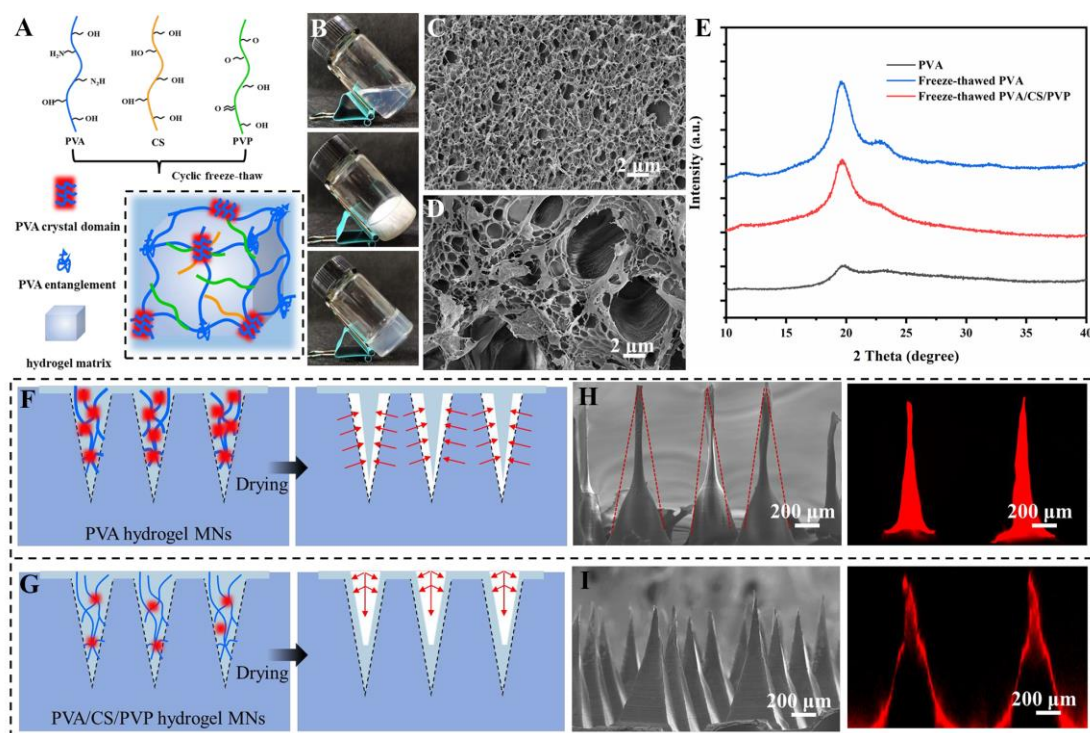
Figure 2. The formation mechanism of hollow-adjustable polymer MNs. Cross-linking mechanism of the composite hydrogel matrix of MNs after freeze-thaw treatment (A), optical images of the composite hydrogel matrix of MNs before and after freeze-thaw treatment (B), SEM images of PVA (C) and the PCP composite hydrogel (D), XRD patterns PVA powder, freeze-thawed PVA and freeze-thawed PCP composite hydrogels (E), schematic diagram of hollow-adjustable polymer MNs during freeze-thaw process (F and G), and SEM images and fluorescence field images of MNs made from dried PVA and PCP composite hydrogels (I).

To determine the optimal proportion of composite matrix, different MNs are prepared by varying compositions of PVA, CS and PVP. Figure S3 displays the shape and structure of resultant MNs made from various compositions. The MNs array structure remains intact using PVA and PVP as the matrix with the mass ratio of 4:1 (Figure S3A). No notable cavity structure can be formed. However, adding a small

amount of CS into matrix with a mass ratio of PVA:CS:PVP = 4:1:1, the resultant

MNs exhibit a cavity structure at the center while still maintaining a complete

pyramid-shape (Figure S3B). Further increasing the amount of CS in matrix with

mass ratio of PVA:CS:PVP= 4:2:1 and 4:3:1, the cavity structure in the center of MNs

still can be kept, but the relative proportion of MNs with damaged structures is

increased as well (Figures S3C and D). In order to determine the effect of PVP on

MNs structure, the swellings of dried composite hydrogels with different

compositions are tested in PBS solution. As shown in Figure S4, a higher swelling

degree can be observed with increasing the relative content of PVP in the composite

hydrogels while maintaining the mass ratio of PVA and CS at 4:1. To ensure a longer

drug release time and good mechanical strength after penetrating MNs into the skin,

the mass ratio of PVA:CS:PVP = 4:1:1 has been selected as matrix for preparation of

hollow-adjustable MNs.

3.2 Fabrication of hollow-adjustable MNs

The MNs are fabricated using a mixed solution with a ratio of PVA/CS/PVP at

4:1:1. It should be noted that the variations in PCP amount directly affect the drying

shrinkage of MNs, as shown in Figure S5, which determines the size of the MNs'

cavity. A larger PCP amount fills more into the MNs mold during drying, resulting in

smaller cavities after shrinkage. To clarify the correlation between the cavity and PCP

amount, MNs with different sizes of MNs' cavity are fabricated, as shown in Figure

3A. Based on the side and 3D views of the MNs, the size of the cavity is inversely

correlated to the amount of PCP. Specifically, MNs prepared by adding ~2 mL

solution of PCP exhibit the most largest cavity volume after drying, whereas MNs prepared by adding ~8 mL solution of PCP exhibit the smallest cavity volume. As shown in Figure 3B, the height of the cavity can be decreased from 596 μm to 195 μm by controlling the added amount of PCP from 2 to 8 mL, which provides a new way to adjust the cavity size of hollow MNs and thus regulating the drug loading capacity of MNs.
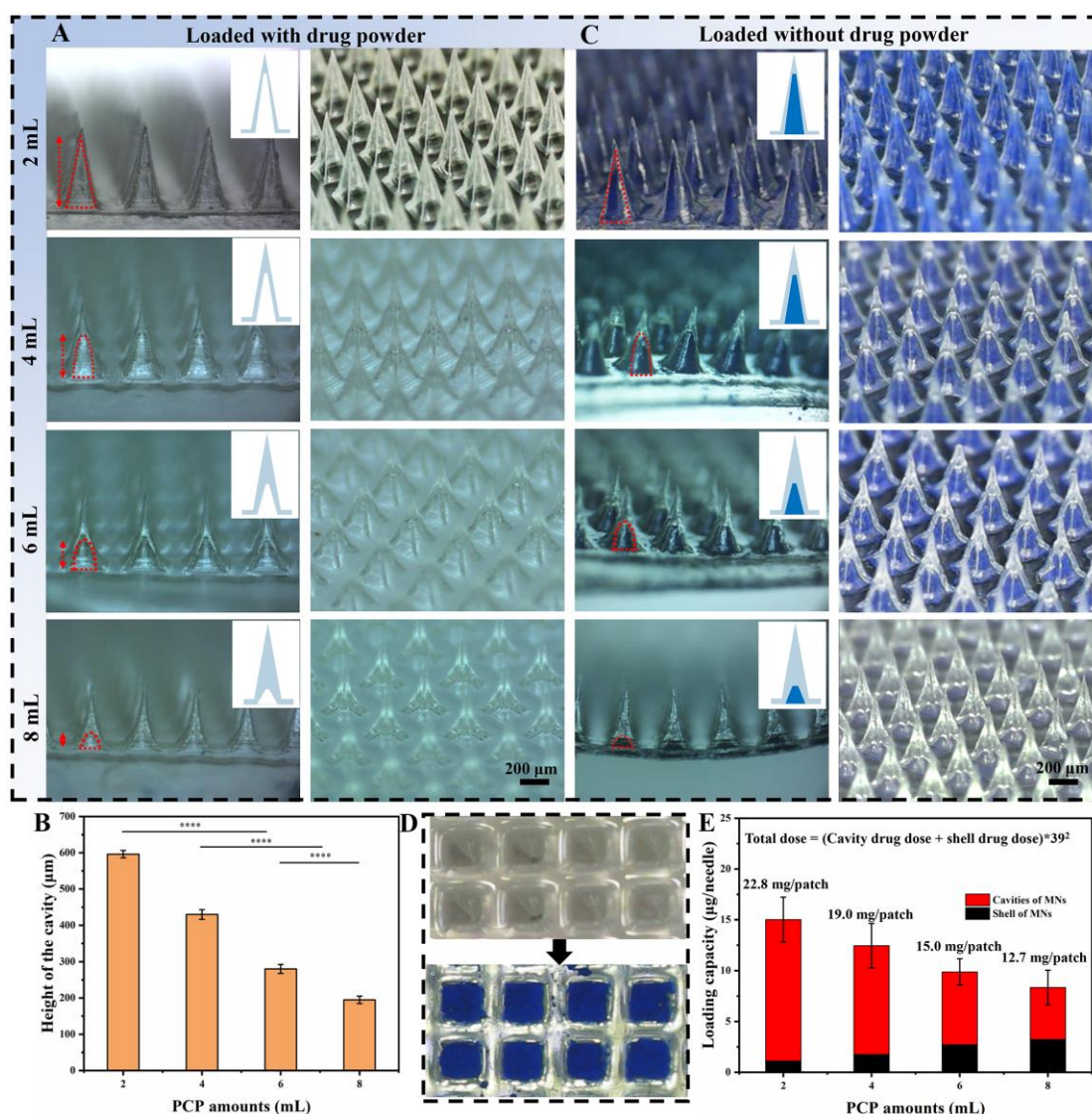
Figure 3. Optical images of loaded without drug powder MNs prepared with different PCP amounts (2, 4, 6, and 8 mL) (A). The height of vacant volume according to increasing backing thickness (B). Optical images of loaded with drug powder MNs prepared with different PCP amounts (2, 4, 6, and 8 mL) (C). Top view before and after MNs filling of drug powder (D). The loading capacity of metformin (E).

To evaluate the drug loading, metformin replaced by Prussian Blue (PB) is used to load into the MNs cavity for convenience observation. The side view and 3D view of hollow MNs after drug loading are shown in Figure 3C. It can be observed that PB is effectively filled into cavities of MNs without any leakage. From the top-view of the drug-encapsulated MNs, it can be found that PB has been successfully filled into the cavity without any loss in the substrate layer (Figure 3D).

The cavity inside the MNs provides a superior site for drug loading, thereby significantly increasing the drug loading capacity in comparison with traditional solid MNs. The amount of drug loading of the MNs is tested through UV curve comparison method. As shown in Figure 3E, the amount of drug loading in the MNs is increased by increasing the cavity size of the hollow MNs. The maximum drug loading amount in MNs is 25.9 mg/patch (17.02 ng/needle) for MNs-2. The total drug loading amount can be adjusted from 25.9 to 15.7 mg/patch according to the size of the cavity inside the MNs.

The PCL hydrophobic shell is coated on the surface of hollow-adjustable MNs through a hot-melting route, enabling the delay of drug release by adjusting the coverage height. As illustrated in Figure 4A, there are four stages for forming the PCL shell: dipping in melt PCL and inversion (a1), partial coverage (a2), complete coverage by PCL (a3), and exposing the needle tips (a4). Figure 4B shows the digital images of MNs at the above different stages. For convenience observation, PCL stained by red-dye R6G is used to wrap MNs. MNs with glossy surfaces are vertically

lifted on the patch before dipping in the hot-melt PCL. While the red-melt PCL drops can be observed on the top of needle tips. Maintaining the temperature above the melting point of PCL (~60 °C) for a certain period, the PCL shell-layer will be formed and solidified around MNs due to its flowing down under the gravity effect.

For better observation of the structure of the as-fabricated MNs with hollow structure, FITC (green) and R6G (red) are utilized to stain the PCL outer-shell and PCP middle-shell, respectively. Laser confocal observation is performed to visualize the prepared MNs, and the corresponding fluorescence images are depicted in Figure 4C. The pyramid-like MNs with green and red fluorescence can be clearly observed, and the color of MNs becomes yellow in the merged image. The side-view images of MNs show the green and red fluorescence shells, and the inner black area represents the cavity of hollow MNs. The overall structure of the MNs with different height cross-sections is further analyzed using laser confocal top-down tomography, as shown in Figure 4D. Only the red fluorescence dot of the solid area of the PCP needle tip can be observed with height cross-sections at 150 μm due to the flowing down of excessive melt PCL and thus the exposure of PCP middle-shell. However, the red fluorescence areas are overlapped by green fluorescence to form yellow fluorescence square-rings at the deeper cross-sections from 250 to 650 μm, demonstrating the formation of the cavity structure in the MNs. This unique structure enables each part of MNs to perform different roles. The internal cavity can be used to load drugs, the inner PCP shell provides sufficient mechanical strength for hollow MNs, and the outermost PCL shell-layer can regulate the drug release rate after insertion into skin.

In addition, the height of the PCL shell-layer outside of hollow MNs can also be adjusted by controlling the time of hot-melt-standing. As shown in Figure 4E, the MNs is fully enveloped by PCL at the initial stage (e1), After hot-melt-standing for 30 min, a small portion of the needle tip is exposed, resulting in the height of PCL shell-layer reduction to ~600 μm (e2). And the height of PCL shell-layer can be further decreased to ~200 μm after 1 h (e3). The morphology of MNs is almost returned to its original state after 2 h hot-melt-standing (e4).
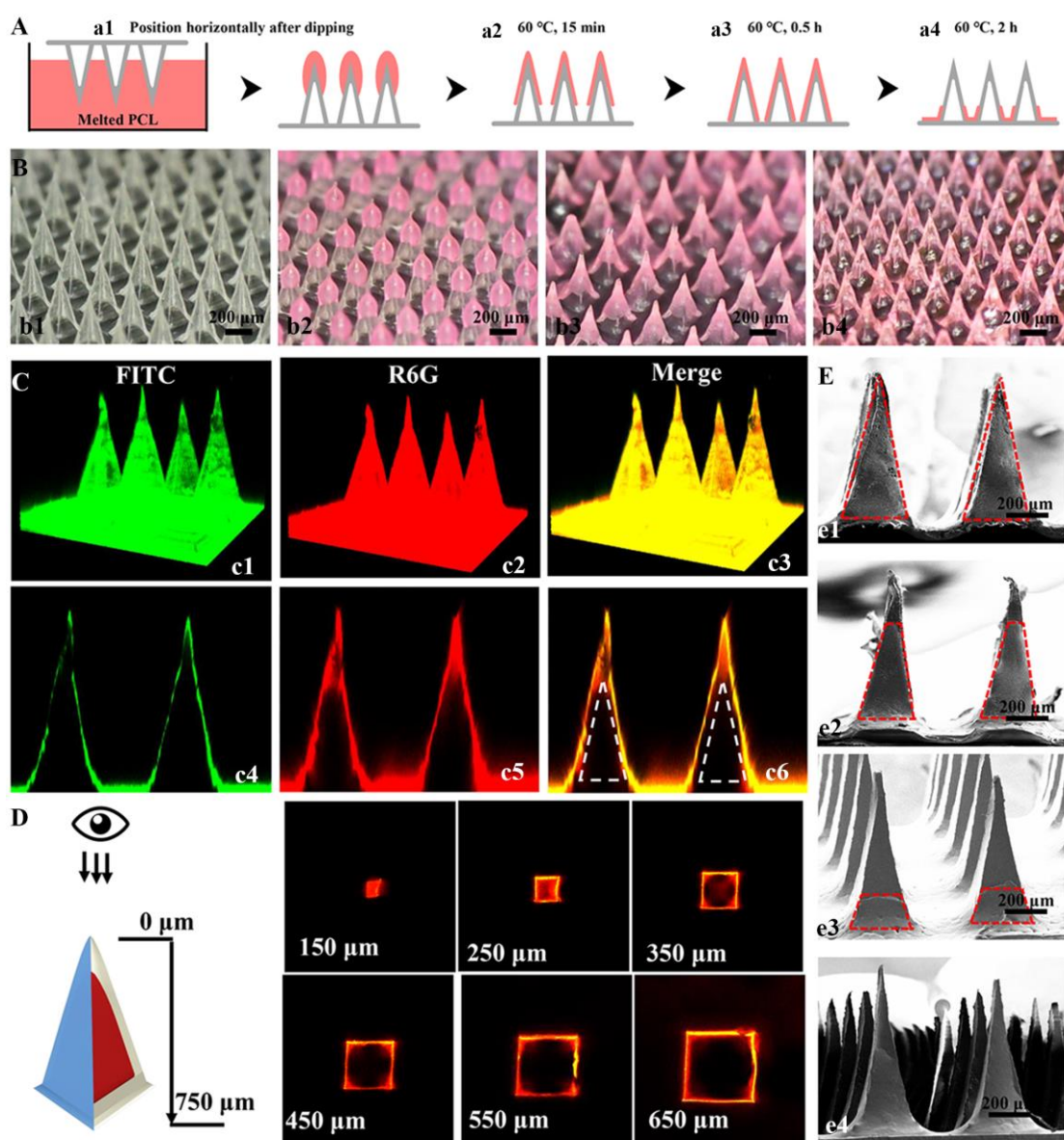
Figure 4. The process of preparing PCL hydrophobic shell of MNs (B): initial state (b1),

dipped in PCL (b2), partially covered (b3) and fully covered by PCL (b4). Laser confocal images of three-layer core-shell MNs (C). Schematic and fluorescence images of laser confocal tomography for three-layer core-shell MNs (D). SEM images of PCL shells MNs with different heights (e1: 750 μm, e2: 500 μm, e3: 200 μm, e4: 0 μm) (E).

### 3.3 Mechanical and insertion properties of MNs

To evaluate the mechanical characteristics of MNs, the fracture strength is tested by an universal material testing machine, as shown in Figure 5A. At a compression displacement of 400 μm, the hollow MNs without drug loading and those protected by a PCL shell-layer exhibit greater susceptibility to being pressed down by the probe in comparison to the hollow MNs loaded with a drug and/or protected by PCL shell-layer, all under the identical measurement conditions. The failure force of drug-unloaded hollow MNs is ~0.082 N/needle, whereas the hollow MNs with loading of drug and/or protecting by PCL shell-layer as the probe pressure reaches 0.101 and 0.105 N/needle, which is higher than mechanical strength requirement to penetrate the skin [70].

In addition, no broken MNs except from slight bending of needle tips can be found after compression tests, implying the toughness of the as-fabricated MNs (Figure 5B). In addition, the cavity size of hollow MNs also affects the mechanical characteristics of MNs. The failure force of drug-unloaded hollow MNs range from ~0.105 to 0.334 N/needle as decreasing the cavity size in MNs. The hollow MNs with a smaller cavity size result a higher mechanical strength (Figure 5C).

Using parafilm (~128 μm each layer) as model for skin insertion test, the holes will be created if MNs can effectively penetrate these parafilm. As shown in Figure 5D and E, nearly 100% MNs with the smallest cavity size can effectively penetrate

three layers of membranes compared to the one with the largest cavity size (~57 %). The hollow MNs with small cavity sizes exhibit the higher mechanical insertion feature. In addition, no fracture or depression has been observed for the hollow MNs after insertion (Figure 5F). In order to understand the adequate penetration depth of MNs in real skin, R6G-dyed MNs are administered onto porcine skin. As shown in Figure 5G, the skin surface reveals a complete array of red spots that correspond to the MNs puncture sites, showing that all MNs are inserted into the skin. Histological sections in Figure 5H clearly demonstrate that R6G-dyed MNs arrowheads (red) have been completely inserted and embedded within the skin tissue with a maximum insertion depth of ~450 μm. The red fluorescence only can be observed near the needles tips after inserting the MNs into the skin for 10 min. After insertion for 2 h, the red fluorescence can be detected at the deeper tissue besides the peripheral region of MNs (Figure S6). These results indicate that the as-fabricated hollow MNs are capable of piercing the skin without breaking, while also enable drug release and diffusion under the skin.
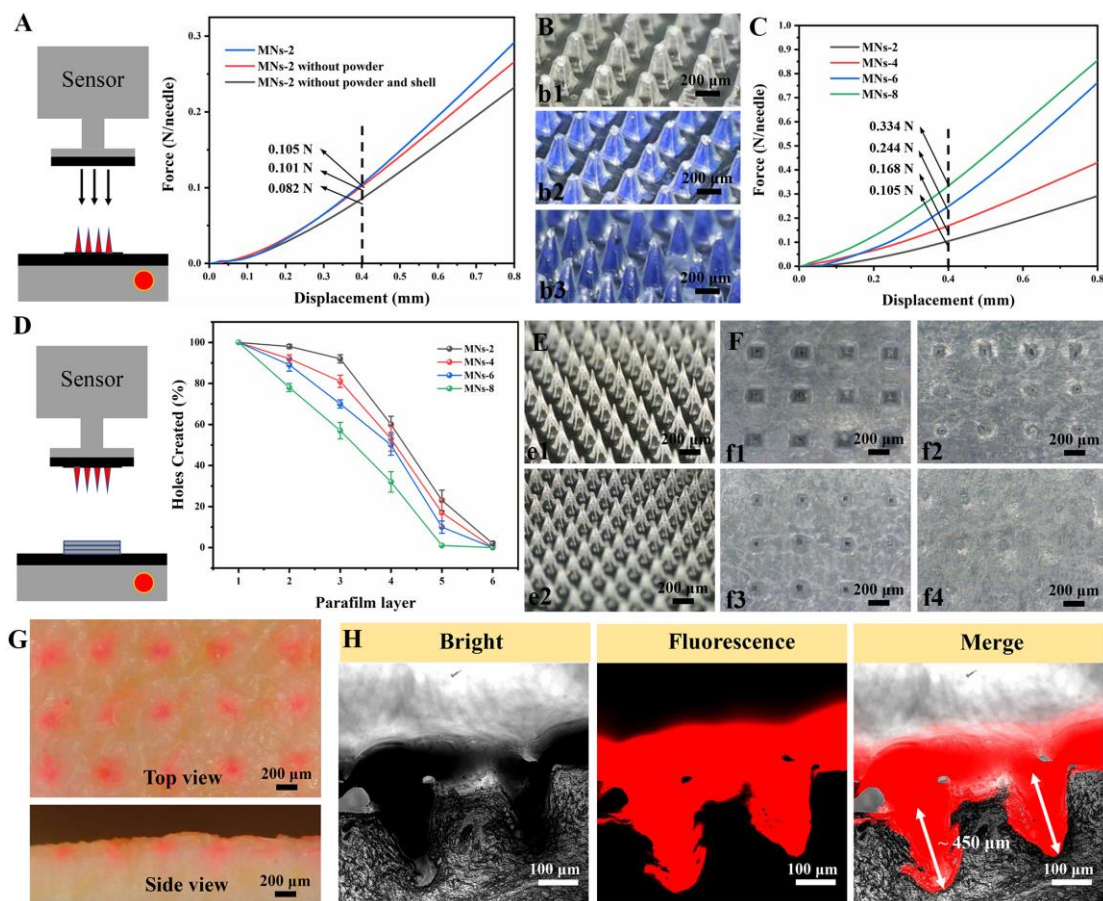
Figure 5. Schematic illustration of the test setup and force-displacement curve of the compression force of different type MNs (A). Optical images of the compressed MNs (B). Force-displacement curve of MNs (MNs-2, MNs-4, MNs-6, MNs-8) (C). Schematic illustration of the test setup and holes created in each parafilm layer by MNs (MNs-2, MNs-4, MNs-6, MNs-8) (D). Optical images before and after MNs insertion into the parafilm (E) and optical images of each layer of parafilm (F). Top and side views of pig skin inserted by MNs (G). Slice images of MNs insertion process (H).

3.4 Cytotoxicity and drug release *in vitro*

Cytotoxicity experiments were conducted to evaluate the biocompatibility of MNs before *in vivo* administration. After co-culture of MNs' extract with 3T3 cells, the cell viability remains above ~80% for the concentrations of MNs extract ranging from 0 to 400 µg/mL, indicating lower cytotoxicity of MNs (Figure 6A). The effective penetration rate of MNs directly affects the accuracy of drug administration. As shown in Figure 6B, ~ 94% MNs-2 in each patch can penetrate porcine skin. The

effective penetration rate can be further increased to ~97% for hollow MNs-4. Almost all MNs could be effectively penetrated porcine skin for those with smaller cavity size. Considering mechanical strength, drug loading capacity, and skin penetration ability, the hollow MNs-6 has been selected for the following *in vivo* experiments.

Drug encapsulation in hollow-MNs was determined to be 15.0 ± 0.5 mg, which was sufficient to deliver a daily therapeutic dose of metformin for *in vivo* experiments. Transdermal release of metformin from hollow-MNs with different height PCL shell-layer into the diffusion cell was monitored for 18 h with MNs pierced into rat skin. The specific formulas of the MNs are shown in Table S1. Specifically, the schematic diagram of MNs#4 is shown in Figure 6C, where the microneedle patch consists of microneedles of three different PCL shell heights, each accounting for one-third of the number of needles. As shown in Figure 6D, the cumulative release amount of metformin in MNs#1 group is ~80% within 4 h and higher than that of MNs#2 and MNs#3 groups, exhibiting a rapid release behavior. The MN#4 group continue to release drugs at a relatively stable rate. After 18 h, the release curves of all groups tend to equilibrium, and about 85.0% of metformin is released into the receptor chamber.
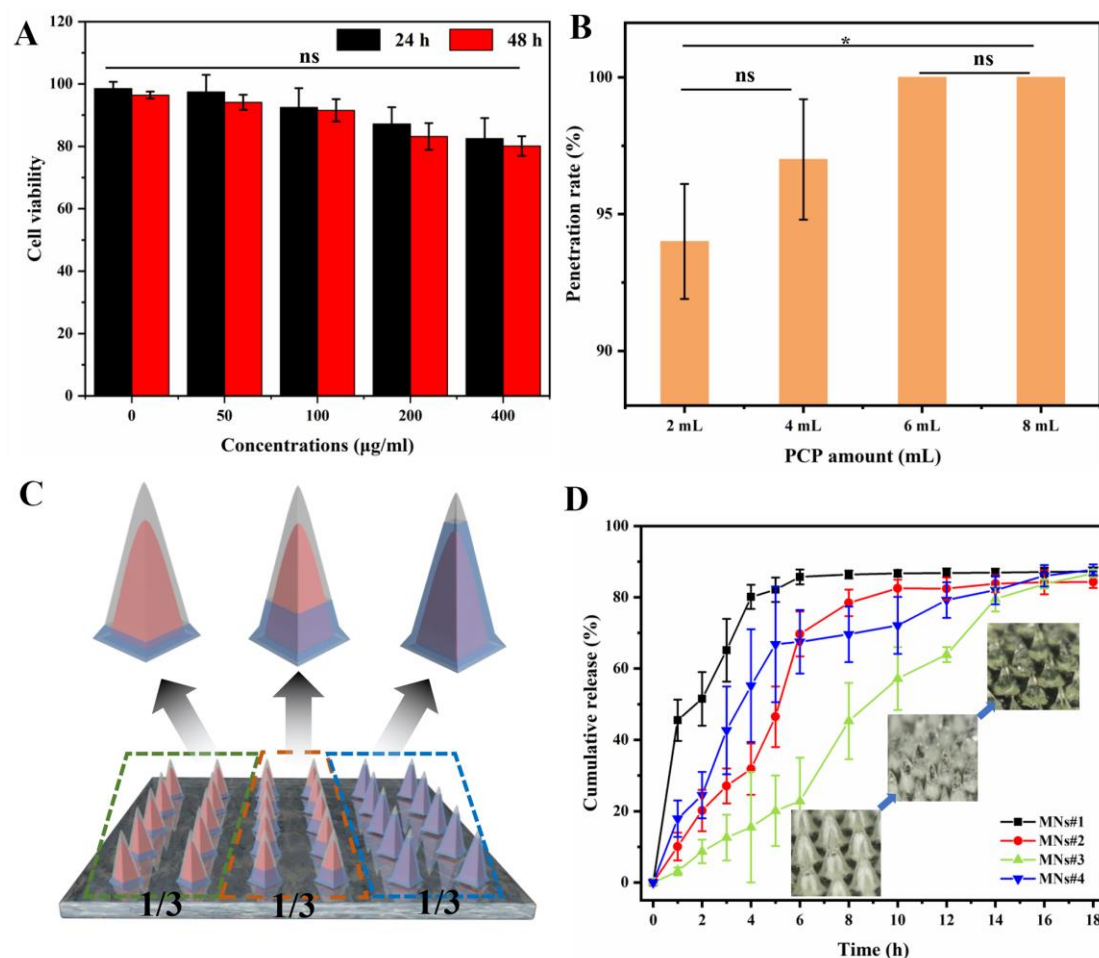
Figure 6. Relative viability of 3T3 cells incubated with extracts of MNs for 24 h and 48 h (A). Penetration rates of MNs on rat skin (B). Schematic diagram of MNs#4 (C). In vitro release of metformin from shell-core MNs in PBS by drug diffusion pool (Illustration: MNs drug release images at different times) (D).

3.5 Hyperglycemia effect *in vivo*

The process of MNs in the treatment of hyperglycemia in a diabetic mice model is depicted in Figure 7A. The BGLs of diabetes rats were evaluated under two feeding modes, including the administration after fasting (①) and the administration without fasting according to "three meals a day"(②). As shown in Figure 7B, in the injection group, the BGLs is decreased rapidly, reaching a minimum of 120.6 mg/dL after injection for 3 h. However, it can be quickly returned to the initial level after a further

10 h. After administration by drug injection, only a short-time hypoglycemic effect window can be observed due to the swift metabolism and excretion. Interestingly, the MNs groups manifest a more pronounced and prolonged hypoglycemic effect. Among them, MN#1 exhibits a fastest drug release behaviour within the initial 4 h, which can be attributed to the absence of PCL shell. Compared to the other MNs groups, this groups results in a more rapid hypoglycemic effect. The lowest BGLs in MNs#1 (140.54 mg/dL) group can be reached after 4 h administration. While, in the case of MNs#2 and MNs#3 groups, the lowest BGLs are 132.47 mg/dL and 156.25 mg/dL after administration for 8 and 12 h due to PCL shell-layer protection. They can maintain BGLs below 200 mg/dL for approximately 4 h. Especially, MNs#4 exhibits a remarkable fast and long-lasting hypoglycemic effect. The lowest BGLs can be reached after 4 h administration, maintaining BGLs below 200 mg/dL for more than 12 h. The significant reduction in BGLs in short-time and long-acting hypoglycemic effect can be contributed to the unique structure of the fabricated hollow MNs. The PCL hydrophobic shell is coated on the surface of hollow-adjustable MNs with exposing the needle tips. The drug loaded in PCP middle-shell is firstly released due to the swelling of MNs after insertion into the skin to achieve a rapid hypoglycemic effect. And the drug loaded in internal cavity will be slowly diffused from MNs after the absorption of body fluids to form a prolonged hypoglycemic effect. The outermost PCL shell-layer can regulate the drug release rate by controlling the size of exposing the needle tips.

In addition, diabetic mice are fed regularly to simulate BGLs changes in our

daily life. As shown in Figure 7C, the BGLs of diabetic mice (~433.98 mg/dL) can be rapidly increased to ~594.12 mg/dL after feeding. After that, it will go back to the initial diabetic level. However, in the case of MNs group, the BGLs can be dropped to 171.7 mg/dL after administration for 5 h, even if BGLs up to ~594.12 mg/dL after feeding. The effective hypoglycemic effect can still be maintained in two continuous feedings after this step. Correspondingly, the concentration of metformin in plasma is also tested using the rat metformin hydrochloride ELISA Kit. As shown in Figure 7D, the plasma metformin concentration is measured at 0.36 ± 0.32 µg/mL in the first hour, reaching the peak value at 3.97 ± 2.18 µg/mL after administration for 3 h and maintaining above 3.0 µg/mL for ~7 h. And it is gradually decreased to 0.62 ± 0.59 µg/mL at 18 h.
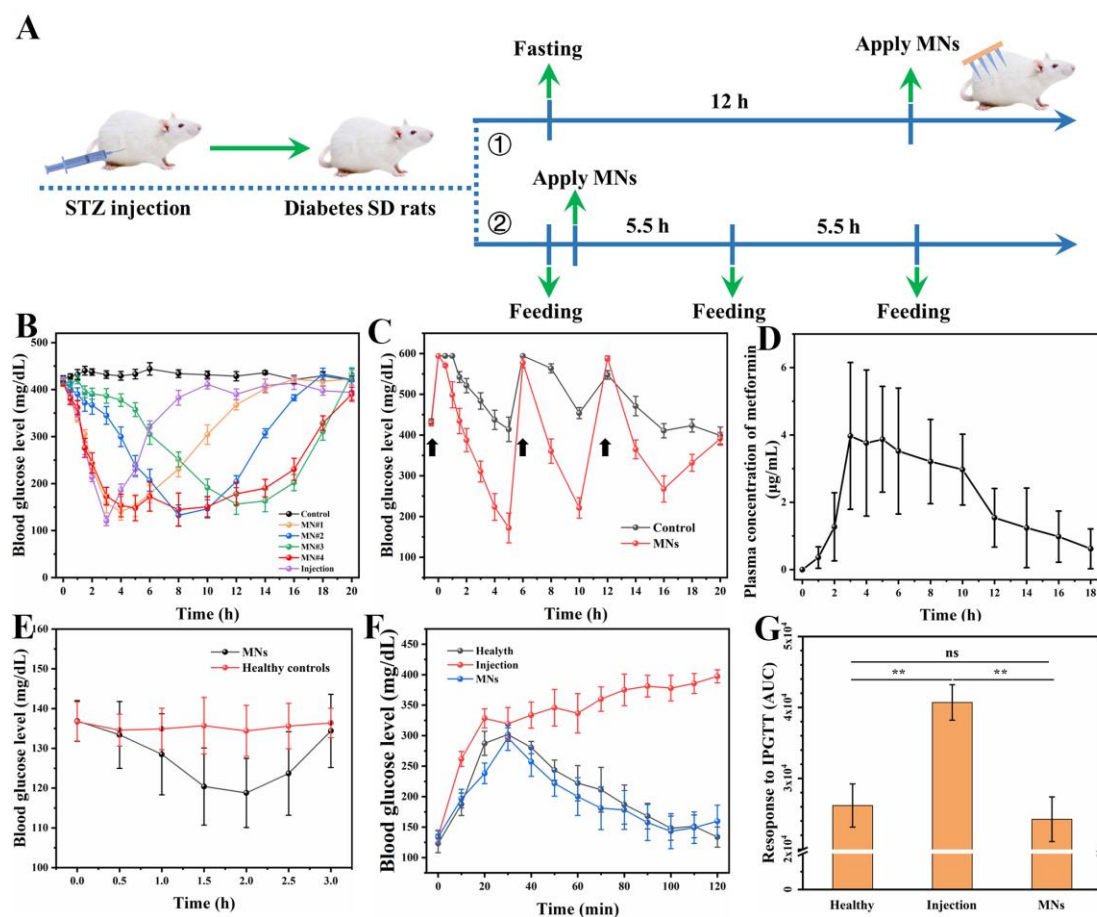
Figure 7. Strategy of MNs patches in the regulation of BLGs in diabetic rats (A). BGLs in diabetic rats after different treatments (B). BGLs in diabetic rats with feeding after MNs#4 treatments, the black arrow represents feeding (C). Plasma drug concentration (D). BGLs in healthy mice treated with MN array patch (E). *In vivo* glucose tolerance test in diabetic rats with treatment of MNs and subcutaneously injected with metformin (F). Responsiveness to intraperitoneal glucose tolerance tests (IPGTTs) that calculated the integral area under the IPGTTs curves from F (G).

To evaluate the hypoglycemic risk associated with the treatment, the BGLs of healthy mice treated with the MNs are monitored. As shown in Figure 7E, the BGLs of rats treated with the MNs only show a slight decrease in healthy mice, indicating no risk of hypoglycemia. Subsequently, intraperitoneal glucose tolerance tests (IPGTTs) are conducted by injecting of glucose [1,37]. IPGTTs were carried out when the BGLs were maintained at normal levels for 1 h after post-administration of MNs#4 or injecting of metformin. As shown in Figure 7F, the BGLs can be rapidly improved after injection of glucose for 20~30 min. For diabetic rats with pre-treatment by injecting of metformin, the BGLs are rapidly enhanced to ~320 mg/dL within 20 min and after that exhibit a continuous and slow increase trend to ~400 mg/dL in 2 h. In the case of diabetic rats with pre-treatment by MNs#4, the BGLs also can be improved to ~300 mg/dL within 30 min. However, they can be returned to the normoglycemic state after 100 min. And the increase trend of BGLs can be effectively suppressed which is almost close to the healthy group. Figure 7G shows responsiveness to IPGTTs that calculated the integral area under the IPGTTs curves from Figure 7F. The diabetic rats group with pre-treatment by MNs#4 is close to the healthy group and displays a 0.5-fold level in comparison with those pre-treatment by injecting of metformin, showing a significant improvement in

glucose tolerance.

3.6 **Histopathological analysis**

Histological analysis is used to further evaluate the safety of MNs administration. Skin tissue samples are collected at three time points for histological analysis, utilizing H&E staining, IL-6 immunohistochemistry, and TUNEL fluorescence staining. Compared with the control group, the skin exhibits micropores resulting from MNs insertion after being treated by MNs for 2 h, and no significant neutrophil infiltration can be observed, as shown in Figure 8A. However, these micropores on the skin surface are hard to be found after 20 h, indicating the realization of self-healing by itself, which is consistent with results obtained from optical microscope, as shown in Figure S7. The thicknesses of the epidermis and skin have no obvious change before and after administration (Figure 8C). The results of IL-6 immunohistochemistry section images are shown in Figures 8B and D. No signature IL-6 expression upregulation can be observed between control and MNs groups. TUNEL immunofluorescence assay is employed to measure cell apoptosis for skin tissue [71-72]. The cell apoptosis percentage is 7.628% in comparison with 7.795% and 8.768% after MNs administration for 2 and 24 h, as shown in Figures 8E and F. There is no signature difference between of them. In addition, acute toxicity was evaluated through H&E staining of sections from key organs. No obvious abnormalities are detected, as shown in Figure 8G.
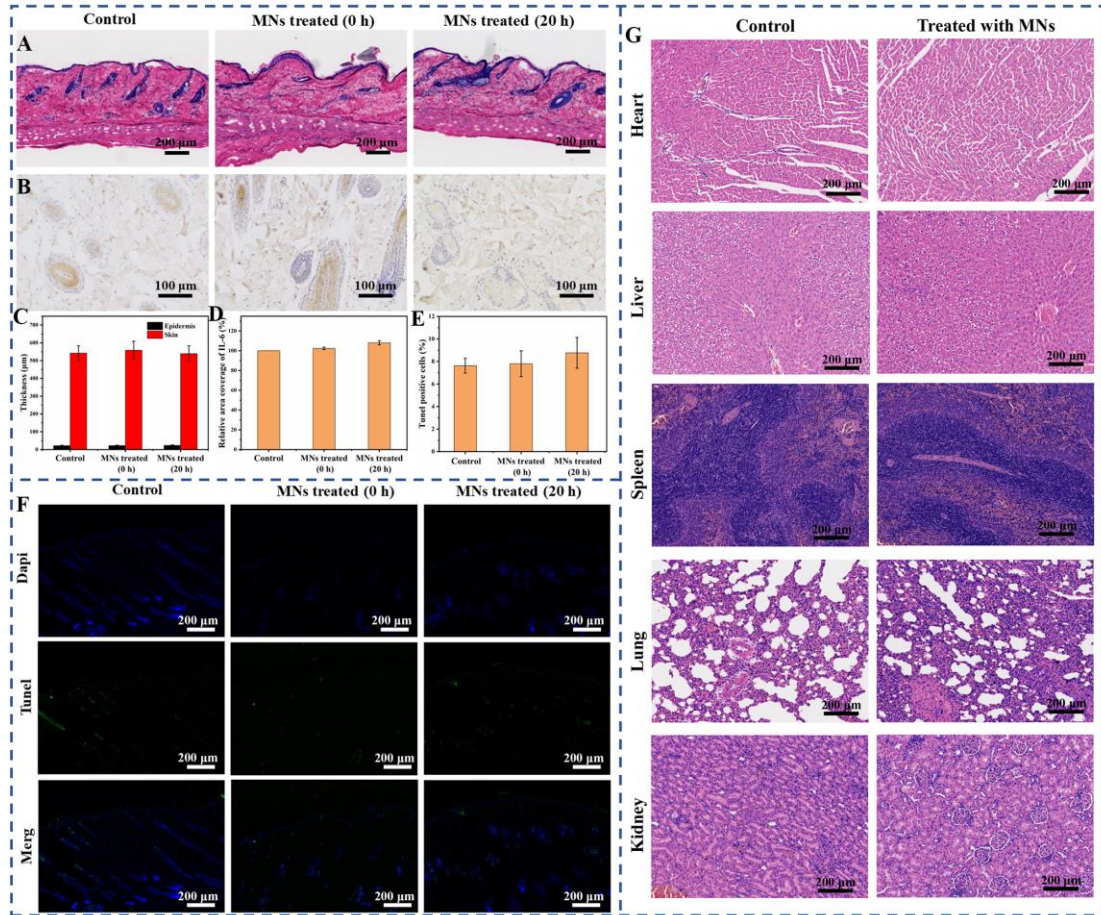
Figure 8. In vivo biocompatibility studies of MNs for diabetes treatment. HE staining sections images (A) and IL-6 immunohistochemistry sections images (B) of the control group and MNs group after treatment for 0 and 20 h. Statistical analysis of the thickness of epidermis and skins treated by MNs (C). Relative area coverage of IL-6 after treatment by MNs (D). The quantitative data of the percentage of TUNEL-positive cells per field (E) and representative images of the TUNEL (F). H&E staining sections of key organs (G)

4 Conclusion

In summary, the hollow-adjustable biocompatible polymer MNs with varying cavity volume were fabricated for improving the drug-loading capacity and extending the hypoglycemic time. The MNs consisted of an outer hydrophobic shell made from polycaprolactone (PCL), an inner hydrogel shell from polyvinyl alcohol/chitosan/polyvinylpyrrolidone (PVA/CS/PVP, PCP), and a hollow cavity for loading metformin drug. This unique structure enables each part of MNs to perform different roles. The internal cavity can be used to load drugs, the inner PCP shell

provides sufficient mechanical strength for hollow MNs, and the outermost PCL shell-layer can regulate the drug release rate after insertion into skin. In addition, the height of the PCL shell-layer outside of hollow MNs can also be adjusted by controlling the time of hot-melt-standing. In addition, the unique structured hollow MNs had sufficient mechanical strength to penetrate skin, offering a sustainable drug release feature. *In vivo* experiments performed on diabetic rat models revealed that the as-fabricated MNs can yield a notable hypoglycemic effect for 14 h after administration without causing the risk of hypoglycemia. These results indicate that the fabricated hollow-adjustable polymer MNs are a potential candidate for transdermal delivery of high-dose drugs.

Author contributions

T. L. designed the MNs; T. L., W. Z., R. W. and X. L. produced MNs patch samples and performed cell and animal experiments; T. L., R. W., Y. S. and G. J. analyzed the results and wrote the draft of manuscript; Y. S. and G. J. conceived the idea and designed the experiments; L. N. and A. S. provided suggestions and commented on the manuscript; K. E. Y., U. E. A. and S. O. S. reviewed the manuscript.

Declaration of Competing Interest

The authors declare that they have no known competing financial interests or personal relationships that could have appeared to influence the work reported in this paper.

Acknowledgments

Reference

[1] Qian Chen, Zhisheng Xiao, Chao Wang, Guojun Chen, Yuqi Zhang, Xudong Zhang, Xiao Han, Jinqiang Wang, Xiao Ye, Mark R. Prausnitz, Song Li, Zhen Gu, Microneedle patches loaded with nanovesicles for glucose transporter-mediated insulin delivery, ACS Nano, 2022, 16(11): 18223-18231.

[2] Tianqi Liu, Yanfang Sun, Guohua Jiang, Wenjing Zhang, Rui Wang, Lei Nie, Amin Shavandi, Khaydar E. Yunusov, Uladzislau E. Aharodnikau, Sergey O. Solomevich, Porcupine-inspired MNs coupled with an adhesive back patching as dressing for accelerating diabetic wound healing, Acta Biomaterialia, 2023, 160: 32-44.

[3] Yangyang Lu, Haojie Yu, Li Wang, Di Shen, Jian Liu, Preparation of phenylboronic acid-based glucose-responsive hydrogels and microneedles for regulated delivery of insulin, European Polymer Journal, 2023, 192(23): 112061.

[4] Zhiyong Zeng, Guohua Jiang, Tianqi Liu, Yanfang Sun, Xueya Zhang, Yanting Jing, Mingjia Feng, Yufei Shi, Fabrication of gelatin methacryloyl hydrogel microneedles for transdermal delivery of metformin in diabetic rats, Bio-Design and Manufacturing, 2021, 4: 902-911.

[5] IDF. Diabetes atlas 10th edition, 2021. https://www.idf.org/. (Accessed June 10 2022).

[6] Tianqi Liu, Guohua Jiang, Gao Song, Yanfang Sun, Xueya Zhang, Zhiyong Zeng, Fabrication of rapidly separable MNs for transdermal delivery of metformin on diabetic rats, Journal of Pharmaceutical Sciences, 2021, 110(8): 3004-3010.

[7] Qilei Wang, Xiaopeng Zhang, Bozhi Chen, Xindong Guo, Dissolvable layered microneedles with core-shell structures for transdermal drug delivery, Materials Science & Engineering C, 2018, 83: 143-147.

[8] Minhui Lu, Lu Fan, Hanxu Chen, Zhuohao Zhang, Yuanjin Zhao, Multifunctional inverse opal microneedle arrays for drug delivery and monitoring, Small, 2022, 18(27): 2201889.

[9] Qingqing Dou, Sing Shy Liow, Enyi Ye, Rajamani Lakshminarayanan, Xian Jun Loh, Biodegradable thermogelling polymers: working towards clinical applications, Advanced Healthcare Materials, 2014, 3(7): 977-988.

[10] Weijiang Yu, Guohua Jiang, Depeng Liu, Lei Li, Zaizai Tong, Juming Yao, Xiangdong Kong, Transdermal delivery of insulin with bioceramic composite microneedles abricated by gelatin

and hydroxyapatite, Materials Science and Engineering C, 2017, 73: 425-428.

[11] Rui Wang, Han Wang, Guohua Jiang, Yanfang Sun, Tianqi Liu, Lei Nie, Amin Shavandi, Khaydar E Yunusov, Uladzislau E Aharodnikau, Sergey O Solomevich, Transdermal delivery of allopurinol on acute gout rats via polymer MNs for regulation of blood uric acid levels, Biomaterials Science, 2023, 11: 1704-1713.

[12] Mingjia Feng, Guohua Jiang, Yanfang Sun, Uladzislau E. Aharodnikau, Khaydar E. yunusov, Tianqi Liu, Zhiyong Zeng, Sergey O. Solomevich, Integration of metformin-loaded mesoporous bioactive glass nanoparticles and free metformin into polymer microneedles for transdermal delivery on diabetic rats, Inorganic Chemistry Communications, 2022, 144: 109896.

[13] Wenxuan Li, Xiaopeng Zhang, Bozhi Zhang, Wenmin Fei, Yong Cui, Canyang Zhang, Xindong Guo, An update on microneedle-based systems for diabetes, Drug Delivery and Translational Research, 2022, 12: 2275-2286.

[14] Jill Ziesmer, Justina Venckute Larsson, Georgios A. Sotiriou, Hybrid microneedle arrays for antibiotic and near-IR photothermal synergistic antimicrobial effect against Methicillin-Resistant Staphylococcus aureus, Chemical Engineering Journal, 2023, 462(15): 142127.

[15] Tânia Moniz, Sofia A Costa Lima, Salette Reis, Marine polymeric microneedles for transdermal drug delivery, Carbohydrate Polymers, 2021, 266(15): 118098.

[16] Xingyu Jiang, Wenzheng Xia, Jiaxing Pan, Wenfang Yang, Shunan Zhang, Chunming Li, Tao Zan, Yi Lai, Zhiai Xu, Haijun Yu, Engineered microneedle systems for topical cancer therapy, Applied Materials Today, 2023, 31: 101774.

[17] Yanjun Zhou, Luan Jia, Di Zhou, Gang Chen, Qiang Fu, Ning Li, Advances in microneedles research based on promoting hair regrowth, Journal of Controlled Release, 2023, 353: 965-974.

[18] Gao Song, Yanfang Sun, Tianqi Liu, Xueya Zhang, Zhiyong Zeng, Ruofan Wang, Pengfei Li, Changhai Li, Guohua Jiang, Transdermal delivery of Cu-doped polydopamine using microneedles for photothermal and chemodynamic synergistic therapy against skin melanoma, Chemical Engineering Journal, 2021, 426(15): 130790.

[19] Zhiyong Zeng, Guohua Jiang, Yanfang Sun, Uladzislau E. aharodnikau, Khaydar E. Yunusov, Xiaofei Gao, Tianqi Liu, Sergey O. Solomevich, Rational design of flexible microneedles coupled with CaO_2@PDA-loaded nanofiber films for skin wound healing on diabetic rats,

Biomaterials Science, 2022, 10: 5326-5339.

[20] Tianqi Liu, Guohua Jiang, Gao Song, Jiangying Zhu, Yuhui Yang, Fabrication of separable MNs with phase change coating for NIR-triggered transdermal delivery of metformin on diabetic rats, Biomedical Microdevices, 2020, 22: 12.

[21] Peipei Yang, Chao Lu, Wangbing Qin, Minglong Chen, Guilan Quan, Hu Liu, Lili Wang, Xuequn Bai, Xin Pan, Chuanbin Wu, Construction of a core-shell microneedle system to achieve targeted co-delivery of checkpoint inhibitors for melanoma immunotherapy, Acta Biomaterialia, 2020, 104: 147-157.

[22] Zhenzhen Qi, Xiaosheng Tao, Guohongfang Tan, Bin Tian, Lehao Zhang, Subhas C. Kundu, Shenzhou Lu, Electro-responsive silk fibroin microneedles for controlled release of insulin, International Journal of Biological Macromolecules, 2023, 242: 124684.

[23] Bin Xu, Qinying Cao, Yang Zhang, Weijiang Yu, Jiangying Zhu, Depeng Liu, Guohua Jiang, Microneedles integrated with ZnO quantum-dot-capped mesoporous bioactive glasses for glucose-mediated insulin delivery, ACS Biomaterials Science & Engineering, 2018, 4: 2473-2483.

[24] Divya Sharma, Jagdish Singh, Long-term glycemic control and prevention of diabetes complications in vivo using oleic acid-grafted-chitosan-zinc-insulin complexes incorporated in thermosensitive copolymer, Journal of Controlled Release, 2020, 323(10): 161-178.

[25] Xiang Chen, Haojie Yu, Li Wang, Di Shen, Yu Wang, Yichuang Hong, Glucose-responsive microneedle patch with variable crosslinking density and flexible core-shell structure for insulin delivery, Advanced Materials Technologies, 2023: 2202124.

[26] Zeqiang Zhao, Baoli Zhang, Huaqing Chu, Ling Liang, Bozhi Chen, Hui Zheng, Xindong Guo, A high-dosage microneedle for programmable lidocaine delivery and enhanced local long-lasting analgesia, Biomaterials Advances, 2022, 133: 112620.

[27] Wei Li, Richard N Terry, Jie Tang, Meihua R Feng, Steven P Schwendeman, Mark R Prausnitz, Rapidly separable microneedle patch for the sustained release of a contraceptive, Nature Biomedical Engineering, 2019, 3: 220-229.

[28] Jiaxin Cao, Yang Liu, Zhenzhen Qi, Xiaosheng Tao, Subhas C. Kundu, Shenzhou Lu, Sustained release of insulin from silk microneedles, Journal of Drug Delivery Science and Technology, 2022, 75: 103611.

[29] Jicheng Yu, Jinqiang Wang, Yuqi Zhang, Guojun Chen, Weiwei Mao, Yanqi Ye, Anna R. Kahkoska, John B. Buse, Robert Langer, Zhen Gu, Glucose-responsive insulin patch for the regulation of blood glucose in mice and minipigs, Nature Biomedical Engineering, 2020, 4: 499-506.

[30] Weijiang Yu, Guohua Jiang, Yang Zhang, Depeng Liu, Bin Xu, Junyi Zhou, Near-infrared light triggered and separable microneedles for transdermal delivery of metformin in diabetic rats, Journal of Materials Chemistry B, 2017, 5: 9507-9513.

[31] Haichuan Peng, Yan Zhou, Chuxi Zhang, Manyu Wang, Siyu Zhao, Yingying Xu, Wei Zhang, Hongbo Xin, Xiaolei Wang, An accurate and dual-effective body slimming method through a soluble microneedle patch with variable temperature, Journal of Materials Chemistry B, 2021, 9: 421-427.

[32] Wei Hu, Xiaowen Bai, Yaping Wang, Zhentao Lei, Haipeng Luo, Zaizai Tong, Upper critical solution temperature polymer-grafted hollow mesoporous silica nanoparticles for near-infrared-irradiated drug release, Journal of Materials Chemistry B, 2019, 7: 5789-5796.

[33] Xiaoxuan Zhang, Guopu Chen, Xiao Fu, Yuetong Wang, Yuanjin Zhao, Magneto-responsive microneedle robots for intestinal macromolecule delivery, Advanced Materials, 2021, 33(44): 2104932.

[34] Xiangjia Li, Weitong Shan, Yang Yang, Dylan Joralmon, Yizhen Zhu, Yiyu Chen, Yuan Yuan, Han Xu, Jiahui Rong, Rui Dai, Qiong Nian, Yang Chai, Yong Chen, Limpet tooth-inspired painless microneedls fabricated by magnetic field-assisted 3D printing, Advanced Functional Materials, 2021, 31(5): 2003725.

[35] Moonjeong Bok, Yunwoo Lee, Daehoon Park, Sangho Shin, Zhi-Jun Zhao, Boyeon Hwang, Soon Hyoung Hwang, So Hee Jeon, Joo-Yun Jung, Sung Ha Park, Junghyo Nah, Eunju Lim, Jun-Ho Jeong, Microneedles integrated with a triboelectric nanogenerator: an electrically active drug delivery system, Nanoscale, 2018, 10: 13502-13510.

[36] Xiaojin Luo, Qi Yu, Yiqun Liu, Weixin Gai, Le Ye, Li Yang, Yue Cui, Closed-loop diabetes minipatch based on a biosensor and an electroosmotic pump on hollow biodegradable microneedles, ACS Sensors, 2022, 7(5): 1347-1360.

[37] Jinqiang Wang, Yanqi Ye, Jicheng Yu, Anna R. Kahkoska, Xudong Zhang, Chao Wang, Wujin Sun, Ria D. Corder, Zhaowei Chen, Saad A. Khan, John B. Buse, Zhen Gu, Core-shell

microneedle gel for self-regulated insulin delivery, ACS Nano, 2018, 12(3): 2466-2473.

[38] Smita Joel, Kendrick B Turner, Sylvia Daunert, Glucose recognition proteins for glucose sensing at physiological concentrations and temperatures, ACS Chemical Biology, 2014, 9(7): 1595-1602.

[39] Chao Wang, Yanqi Ye, Wujin Sun, Jicheng Yu, Jingqiang Wang, David S. Lawrence, John B. Buse, Zhen Gu, Red blood cells for glucose-responsive insulin delivery, Advanced Materials, 2017, 29(18): 1606617.

[40] Bin Xu, Qinying Cao, Yang Zhang, Weijiang Yu, Jiangying Zhu, Depeng Liu, Guohua Jiang, Microneedles integrated with ZnO quantum-dot-capped mesoporous bioactive glasses for glucose-mediated insulin delivery, ACS Biomaterials Science & Engineering, 2018, 4: 2473-2483.

[41] Bin Xu, Guohua Jiang, Weijiang Yu, Depeng Liu, Yang Zhang, Junyi Zhou, Shiqing Sun, Yongkun Liu, H_2O_2-responsive mesoporous silica nanoparticles integrated with microneedle patches for the glucose-monitored transdermal delivery of insulin, Journal of Materials Chemistry B, 2017, 5: 8200-8208.

[42] Zhou Ye, Yuanhui Xiang, Thomas Monroe, Sihan Yu, Ping Dong, Sijie Xian, Matthew J Webber, Polymeric microneedle arrays with glucose-sensing dynamic-covalent bonding for insulin delivery, Biomacromolecules, 2022, 23(10): 4401-4411.

[43] Siyuan Chen, Takuya Miyazaki, Michiko Itoh, Hiroko Matsumoto, Yuki Moro-oka, Miyako Tanaka, Yuji Miyahara, Takayoshi Suganami, Akira Matsumoto, Temperature-stable boronate gel-based microneedle technology for self-regulated insulin delivery, ACS Applied Polymer Materials, 2022, 2(7): 2781-2790.

[44] Junyou Li, Yunhao Feng, Yuting He, Liufu Hu, Ling Liang, Zeqiang Zhao, Bozhi Chen, Xindong Guo, Thermosensitive hydrogel microneedles for controlled transdermal drug delivery, Acta Biomaterialia, 2022, 153: 308-319.

[45] Pei Zhang, Yan Zhang, Chenguang Liu, Polymeric nanoparticles based on carboxymethyl chitosan in combination with painless microneedle therapy systems for enhancing transdermal insulin delivery, RSC Advances, 2020, 10: 24319-24329.

[46] Yun Fu, Peng Liu, Meng Chen, Tongxia Jin, Huijing Wu, Mingyang Hei, Congrong Wang, Yufang Xu, Xuhong Qian, Weiping Zhu, On-demand transdermal insulin delivery system for

type 1 diabetes therapy with no hypoglycemia risks, Journal of Colloid and Interface Science, 2022, 605: 582-591.

[47] Qida Zong, Ranan Guo, Naijun Dong, Guixia Ling, Peng Zhang, Design and development of insulin microneedles for diabetes treatment, Drug Delivery and Translational Research, 2022, 12: 973-980.

[48] Eman M. Migdadi, Aaron J. Courtenay, Ismaiel A. Tekko, Maelíosa T.C. McCrudden, Mary-Carmel Kearney, Emma McAlister, Helen O. McCarthy, Ryan F. Donnelly, Hydrogel-forming microneedles enhance transdermal delivery of metformin hydrochloride, Journal of Controlled Release, 2018, 285: 142-151.

[49] Suyong Kim, Jaehong Eum, Huisuk Yang, Hyungil Jung, Transdermal finasteride delivery via powder-carrying microneedles with a diffusion enhancer to treat androgenetic alopecia, Journal of Controlled Release, 2019, 316: 1-11.

[50] Suyong Kim, Huisuk Yang, Jahong Eum, Yonghao Ma, Shayan Fakhraei Lahiji, Hyungil Jung, Implantable powder-carrying microneedles for transdermal delivery of high-dose insulin with enhanced activity, Biomaterials, 2020, 232: 119733.

[51] Khanh T. M. Tran, Tyler D. Gavitt, Nicholas J. Farrell, Eli J. Curry, Arlind B. Mara, Avi Patel, Lindsey Brown, Shawn Kilpatrick, Roxana Piotrowska, Neha Mishra, Steven M. Szczepanek, Thanh D. Nguyen, Transdermal microneedles for the programmable burst release of multiple vaccine payloads, Nature Biomedical Engineering, 2021, 5: 998-1007.

[52] Wei Li, Jonathan Yuxuan Chen, Richard N. Terry, Jie Tang, Andrey Romanyuk, Steven P. Schwendeman, Mark R. Prausnitz, Core-shell microneedle patch for six-month controlled-release contraceptive delivery, Journal of Controlled Release, 2022, 347: 489-499.

[53] Bozhi Chen, Liqin Zhang, Yiyun Xia, Xiaopeng Zhang, Xindong Guo, A basal-bolus insulin regimen integrated microneedle patch forintraday postprandial glucose control, Science Advances, 2020, 6(28): eaba7260.

[54] Rongyan He, Yan Niu, Zedong Li, Ang Li, Huayuan Yang, Feng Xu, Fei Li, A hydrogel microneedle patch for point-of-care testing based on skin interstitial fluid, Advanced Healthcare Materials, 2020, 9: 1901201.

[55] Yu Wang, Haojie Yu, Li Wang, Jian Hu, Jingyi Feng, Di Shen, Yichuan Hong, Jinyi Liu, Dingning Chen, Microneedles with two-stage glucose-sensitive controlled release for long-term

insulin delivery, ACS Biomaterials & Engineering, 2023, 9(5): 2534-2544.

[56] Vladislav Rac, Steva Lević, Bojana Balanč, Beatriz Olalde Graells, Goran Bijelić, PVA Cryogel as model hydrogel for iontophoretic transdermal drug delivery investigations. Comparison with PAA/PVA and PAA/PVP interpenetrating networks, Colloids and Surfaces B: Biointerfaces, 2019, 180(1): 441-448.

[57] Sixing Yang, Fei Wu, Jianguo Liu, Guorong Fan, William Welsh, Hua Zhu, Tuo Jin, Phase-transition microneedle patches for efficient and accurate transdermal delivery of insulin, Advanced Functional Materials, 2015, 25(29): 4633-4641.

[58] Christian Gornik, Injection moulding of parts with microstructured surfaces for medical applications, Macromolecular Symposia, 2004, 217(1): 365-374.

[59] Xiaoyan Zhang, Wenlong Huo, Shu Yan, Yugu Chen, Ke Gan, Jingjing Liu, Jinlong Yang, Innovative application of PVA hydrogel for the forming of porous Si_3N_4 ceramics via freeze-thaw technique, Ceramics International, 2018, 44(11): 13409-13413.

[60] Yosthanase Tassanapukdee, Pornpimol Prayongpan, Kriangsak Songsrirote, Removal of heavy metal ions from an aqueous solution by CS/PVA/PVP composite hydrogel synthesized, Environmental Technology & Innovation, 2021, 24: 101898.

[61] P. Sankarganesh, V. Parthasarathy, A. Ganesh Kumar, S. Ragu, M. Saraniya, N. Udayakumari, R. Anbarasan, Preparation of cellulose-PVA blended hydrogels for wound healing applications with controlled release of the antibacterial drug: an in vitro anticancer activity, Biomass Conversion and Biorefinery, 2022, 1: 1-11.

[62] William Xaveriano Waresindo, Halida Rahmi Luthfianti, Dhewa Edikresnha, Tri Suciati, Fatimah Arofiati Noor, Khairurrijal Khairurrijal, A freeze–thaw PVA hydrogel loaded with guava leaf extract: physical and antibacterial properties, RSC Advances, 2021, 11: 30156-30171.

[63] Wildan Hanif, Andri Hardiansyah, Ahmad Randy, Lia A.T.W. Asri, Physically crosslinked PVA/graphene-based materials/aloe vera hydrogel with antibacterial activity, RSC Advances, 2021, 11: 29029.

[64] Srikant S. Kulkarni, Arjumand A. Kittur, Mrityunjaya I. Aralaguppi, Mahadevappa Y. Kariduraganavar, Synthesis and characterization of hybrid membranes using poly(vinyl alcohol) and tetraethylorthosilicate for the pervaporation separation of water–isopropanol mixtures,

Journal of Applied Polymer Science, 2004, 94(3): 1304-1315.

[65] T.S. Soliman, S.A. Vshivkov, Effect of Fe nanoparticles on the structure and optical properties of polyvinyl alcohol nanocomposite films, Journal of Non-Crystalline Solids, 2019, 519(1): 119452.

[66] E. Sheha, H. Khoder, T.S. Shanap, M.G. El-Shaarawy, M.K. El Mansy, Structure, dielectric and optical properties of p-type (PVA/CuI) nanocomposite polymer electrolyte for photovoltaic cells, Optik, 2012, 123(13): 1161-1166.

[67] Lianyu Lu, Fubing Peng, Zhongyi Jiang, Jianghui Wang, Poly(vinyl alcohol)/chitosan blend membranes for pervaporation of benzene/cyclohexane mixtures, Journal of Applied Polymer Science, 2006, 101(1): 167-173.

[68] Desheng Liu, Yufei Cao, Pan Jiang, Yixian Wang, Yaozhong Lu, Zhongying Ji, Xiaolong Wang, Weimin Liu, Tough, transparent, and slippery PVA hydrogel led by syneresis, Small, 2023, 19(14): 2206819.

[69] Yuan Yang, Huaqing Chu, Yan Zhang, Lingling Xu, Ruizeng Luo, Hui Zheng, Tailang Yin, and Zhou Li, Rapidly separable bubble microneedle patch for effective local anesthesia, Nano Research, 2022, 15(9): 8336-8344.

[70] Jung-Hwan Park, Mark G. Allen, Mark R. Prausnitz, Biodegradable polymer microneedles: fabrication, mechanics and transdermal drug delivery, Journal of Controlled Release, 2005, 104, 51-66.

[71] Panpan Lu, Qiang Ding, Xin Li, Xiaoyu Ji, Lili Li, Yuhui Fan, Yujia Xia, Dean Tian, Mei Liu, SWELL1 promotes cell growth and metastasis of hepatocellular carcinoma in vitro and in vivo, EBioMedicine, 2019, 48: 100-116.

[72] Jiachen Sun, Xinzhu Liu, Chuanan Shen, Wen Zhang, Yuezeng Niu, Adiponectin receptor agonist AdipoRon blocks skin inflamm-ageing by regulating mitochondrial dynamics, Cell Proliferation, 2021, 54(12): e13155.

.